

# Phase-Field Simulation on the Influence of Cooling Rate on the Solidification Microstructure of Mg-Gd-Y Ternary Magnesium Alloy

Zhao Xueting<sup>1,2</sup>, Shang Shan<sup>1,2</sup>, Zhang Tianxiang<sup>1,2,3</sup>, Zhang Ruijie<sup>3</sup>, Wang Xianfei<sup>4</sup>,  
Li Zhongquan<sup>4</sup>, Han Zhiqiang<sup>1,2</sup>

<sup>1</sup> School of Materials Science and Engineering, Tsinghua University, Beijing 100084, China; <sup>2</sup> Key Laboratory for Advanced Materials Processing Technology (Ministry of Education), Tsinghua University, Beijing 100084, China; <sup>3</sup> Collaborative Innovation Center of Steel Technology, University of Science and Technology Beijing, Beijing 100083, China; <sup>4</sup> Shanghai Spaceflight Precision Machinery Institute, Shanghai 201600, China

**Abstract:** A phase-field model of ternary Mg-Gd-Y magnesium alloy was developed by coupling with the thermodynamics of Mg-Gd-Y system and considering cooling rate for the first time. It was applied to simulate the solidification microstructure and concentration distribution of GW103 (Mg-1.69mol%Gd-1.32mol%Y) alloy at different cooling rates both in one-grain and multigrain simulation cases. Then GW103 alloys were prepared by gravity casting method and characterized to verify the model. Results give new understanding that the GW103 alloy exhibits thick six fold primary dendrite, a few protuberance-like secondary arms and even no higher-order arms, instead of developed dendrite. The ascending cooling rate results in refinement of microstructure of GW103, which exhibits smaller grain size, slimmer primary dendrite and less secondary arms in multigrain simulation case. Besides, higher cooling rate aggravates the solute enrichment and inhomogeneous distribution of Gd and Y in interdendritic area. The simulation and the experimental results are matched well.

**Key words:** phase-field; simulation; magnesium; microstructure; cooling rate

The application of lightweight alloys has increased in the last decade for transportation purposes to reduce mass and energy consumption<sup>[1]</sup>. Magnesium alloys have attracted increasing attention in automotive industry owing to their low density, excellent castability and machinability<sup>[2-4]</sup>. The most widely applied magnesium alloys is Mg-Al system alloy<sup>[2, 5]</sup>, such as AZ91 alloy<sup>[2, 6]</sup>. Recently, magnesium alloys that contain heavy rare earth metals exhibit good performance at room temperature as well as elevated temperature<sup>[7-9]</sup>, among which Mg-Gd-Y alloy is a potential alloy in the field of aerospace<sup>[10-13]</sup>.

It is reported that cooling rate is a crucial parameter in influencing solidification microstructure of Mg-Gd-Y alloy, such as phase constitution, the fraction of secondary

phase<sup>[14, 15]</sup>, grain size<sup>[14]</sup> and segregation<sup>[15]</sup>, and thus deciding the mechanical properties of casting<sup>[14]</sup>. Pang et al.<sup>[14]</sup> studied the influence of cooling rate on the microstructure of sand cast Mg-10Gd-3Y-0.5Zr alloy with the cooling rate varying from 0.7 to 3.61 K/s, and it is found that the average grain size of  $\alpha$ -Mg reduced with the increase of cooling rate. Zhou et al.<sup>[15]</sup> revealed that the increasing cooling rate contributed to the refinement of the grains, and the morphology of primary phases varied from coarse to thin as the cooling rate increased. With the increase of cooling rates which were higher than a critical value, the segregation of solutes in the interdendritic area was reduced, due to the fact that the solid composition is close to the initial composition of alloy.

Received date: November 1, 2019

Foundation item: National Key Research and Development Program of China (2016YFB0701204); National Natural Science Foundation of China (U1737208)

Corresponding author: Han Zhiqiang, Ph. D., Associate Professor, School of Materials Science and Engineering, Tsinghua University, Beijing 100084, P. R. China, Tel: 0086-10-62794616, E-mail: zqhan@tsinghua.edu.cn

Copyright © 2020, Northwest Institute for Nonferrous Metal Research. Published by Science Press. All rights reserved.

With the development of computer technology, using numerical simulation method<sup>[16-22]</sup>, such as cellular automaton (CA)<sup>[18, 19]</sup> or phase-field (PF) method<sup>[20-22]</sup>, to understand and predict the characteristic of alloys during solidification process can effectively promote the research and application of cast magnesium alloys. Phase-field modeling on the basis of solute diffusion, ordering potential and thermodynamic driving force is a powerful tool to simulate and study microstructure evolution during phase transformation<sup>[23-31]</sup>. Generally, the commercial magnesium alloys are based on multi-component systems, and thus the development of a multi-component phase-field model coupled with the corresponding thermodynamics is necessary. A ternary phase-field model for Mg-Al-Sn alloy coupled with corresponding thermodynamics and pressure was established in our previous work<sup>[32]</sup>, and the microsegregation and dendritic growth kinetics of Mg-Al-Sn alloy affected by pressure were investigated. Most investigations regarding the influence of cooling rate on the solidification microstructure of Mg-Gd-Y alloys were executed via experiments, while the phase-field model coupling the thermodynamics of Mg-Gd-Y alloy and taking cooling rate into consideration has not been developed yet to make it possible to investigate the effects of cooling rate on dendritic growth kinetics of Mg-Gd-Y alloy in a numerical approach.

In this work, a phase-field model describing solidification microstructure of Mg-Gd-Y alloy was developed by coupling with the thermodynamics of Mg-Gd-Y alloy and taking cooling rate into consideration. Based on the model, one-grain and multigrain simulation cases were carried out to investigate the dendritic characteristics of GW103 (Mg-1.69mol%Gd-1.32mol%Y) alloy at different cooling rates, and the influence of cooling rate on the morphology of dendrites, including primary dendrites and secondary arms, the grain size and concentration distribution were studied and analyzed. Furthermore, in order to verify the model, GW103 alloys solidified at different cooling rates were prepared by gravity casting method and the microstructure was characterized by optical microscope (OM) and scanning electron microscopy (SEM). The solute distribution was characterized by energy dispersive spectrometer (EDS).

## 1 Phase-field Modeling and Experimental Method

### 1.1 Phase-field model for ternary system

In a system with  $(n+1)$  components, the free energy density ( $f$ ) of  $m$  phase is illustrated as Eq.(1)<sup>[24]</sup>:

$$f^m = (c_{1m}, c_{2m}, \dots, c_{nm}) \quad (1)$$

Where  $c_i$  is the concentration of  $i$ th solute ( $i=1, 2, \dots, n$ ),  $m=L$  or  $S$  represents the liquid or solid phase, respectively. The governing equations of a multicomponent system are explicitly written as Eqs.(2) and (3) for phase field and concentration field respectively<sup>[24]</sup>:

$$M_\phi^{-1} (\partial \phi / \partial t) = \varepsilon^2 \nabla^2 \phi - w g'(\phi) - h_p'(\phi) \cdot [f^S - f^L - \sum (c_{iS} - c_{iL}) \tilde{\mu}_i] \quad (2)$$

$$\partial c_i / \partial t = \nabla \cdot [1 - h_d(\phi)] \sum D_{ij}^L \nabla c_{jL} + \nabla \cdot [\varepsilon (2w)^{-0.5} (c_{iL} - c_{iS})] (\partial \phi / \partial t) (\nabla \phi / |\nabla \phi|) \quad (3)$$

where  $\phi$  is the order parameter which is defined as  $\phi = 0$ ,  $\phi = 1$  and  $0 < \phi < 1$  in the bulk liquid, bulk liquid and the interfacial region between them, respectively.  $c_{iS}$  and  $c_{iL}$  are the composition of solid and liquid of  $i$ th solute, respectively. Eqs.(4) and (5) are equations for solving the governing equation of phase-field model, which means that the concentration  $c_i$  follows the mixture rule, as well as that  $c_{iS}$  and  $c_{iL}$  follow the equal chemical potential condition at a given point in the interfacial region<sup>[24, 33-35]</sup>,

$$c_i = h_r(\phi) c_{iS} + [1 - h_r(\phi)] c_{iL} \quad (4)$$

$$\partial f^S / \partial c_{iS} = \partial f^L / \partial c_{iL} \equiv \tilde{\mu}_i \quad (5)$$

Where  $\tilde{\mu}_i$  is the chemical potential,  $f^S$  and  $f^L$  are the free energy densities of solid and liquid phase.  $g(\phi)$  is the double-well potential which is expressed as  $g(\phi) = \phi^2(1-\phi)^2$ .  $h(\phi)$  distinguished by the subscripts  $p$ ,  $r$  and  $d$  in Eqs.(2)~(4) are monotonous interpolation functions satisfying  $h(\phi) = 0$  and  $h(\phi)=1$ . In this paper, the interpolation functions are expressed by  $h_p(\phi) = \phi^3(10 - 15\phi + 6\phi^2)$  and  $h_d(\phi) = h_r(\phi) = \phi$  which satisfy the symmetry condition. The detailed reasons for the choice of such function forms can be found in Ref.[24].  $D_{ij}^L$  is the diffusivity in liquid phase which varies with temperature. The second term in the right-hand side of Eq.(3) is 'anti-trapping' (AT) current term. The AT current term prevents an abrupt chemical potential jump across the solid-liquid interface relevant to finite interface width in the phase-field model<sup>[24, 36]</sup>.  $w$ ,  $\varepsilon$ , and  $M_\phi$  in Eqs.(2) and (3) represent the height of the parabolic potential, the gradient energy coefficient and the phase field mobility, respectively, expressed as Eqs.(6)~(8)<sup>[33, 37]</sup>:

$$\varepsilon = (6\lambda\sigma/\alpha)^{0.5} \quad (6)$$

$$w = 3\alpha\sigma/\lambda \quad (7)$$

$$M_\phi^{-1} = \varepsilon^3 \sigma^{-1} (2w)^{-0.5} [ \xi_1 (c_{1L}^e, c_{1S}^e) / D_{1i}^L + \xi_2 (c_{2L}^e, c_{2S}^e) / D_{2i}^L ] \quad (8)$$

Where  $\alpha$  is a constant depending on the definition of the interface thickness.  $\alpha \approx 2.94$  when the interface region is defined as  $-\lambda < x < +\lambda$ .  $\sigma$  is interface energy, and  $2\lambda$  is interface width. The anisotropy is introduced into the interface energy as Eq.(9) described<sup>[38]</sup>:

$$\sigma(\theta) = \sigma_0 [1 + \gamma \cos(\eta\theta)] \quad (9)$$

Where  $\sigma_0$  is the isotropic interface energy and  $\gamma$  is the anisotropy strength.  $\eta$  equals 6 for magnesium alloys, which is related to the sixfold crystal structure.  $\theta$  is the angle between the horizontal direction and the normal of the interface which points to the liquid.  $\xi_i$  is a function related to equilibrium composition of solid ( $c_{iS}^e$ ) and liquid ( $c_{iL}^e$ ). The definitions of parameters associated with the phase-field equations can be found in Refs.[24, 33-38] in detail.

### 1.2 Cooling rate

To investigate the influence of cooling rate on solidifica-

tion microstructure of Mg-Gd-Y alloy, the temperature in the model was set as:

$$T^p = T^{p-1} - R_{\text{cooling}} \Delta t \quad p = 1, 2, \dots \quad (10)$$

Where  $T^p$  represents the temperature in current calculation step,  $T^{p-1}$  represents the temperature in last calculation step,  $T^0$  denotes the initial simulation temperature when the calculation step  $p = 1$ ,  $R_{\text{cooling}}$  is cooling rate and  $\Delta t$  is time step. Therefore, the phase-field model considering the influence of cooling rate for ternary magnesium alloy was developed.

### 1.3 Thermodynamics

The thermodynamic model in a multicomponent system can be described as<sup>[39]</sup>:

$$G^m = \sum c_i^0 G_i^m + RT \sum c_i \ln c_i + G^{m,\text{ex}} \quad (11)$$

Where  $i = 1, 2, 3$  represent component Gd, Y and Mg for Mg-Gd-Y ternary system, respectively.  $G^m$  is the Gibbs free energy for solid phase ( $m=S$ ) or liquid phase ( $m=L$ ).  $G_i^m$  is the Gibbs free energy of pure component  $i$ .  $R$  is the gas constant.  $T$  is the temperature. The first term represents the contribution of pure components of the phase to the Gibbs free energy, the second term represents the ideal mixing contribution, and  $G^{m,\text{ex}}$  represents the Gibbs excess energy of mixing described as below:

$$G^{m,\text{ex}} = \sum_{i=1}^2 \sum_{j=i+1}^3 c_i c_j \sum_{v=0}^n [{}^v L_{ij}^m (c_i - c_j)^v] + c_1 c_2 c_3 L^{\text{ter}} \quad (12)$$

Where  ${}^v L_{ij}^m$  and  $L^{\text{ter}}$  are the model parameters. In Mg-Gd-Y system, the Gibbs excess energy of mixing is expressed as follows where the formula unit is J/mol<sup>[40]</sup>.

$$G^{L,\text{ex}} = c_{\text{Gd}} c_{\text{Mg}} [(-36681.3 + 16.2484T) + (34233.8 - 10.7783T)(c_{\text{Gd}} - c_{\text{Mg}}) + (-7352.9)(c_{\text{Gd}} - c_{\text{Mg}})^2] + c_{\text{Gd}} c_{\text{Y}} (-2014.5 + 1.0695T) + c_{\text{Mg}} c_{\text{Y}} [(-41194.9 + 17.5452T) + (-15779.0 + 4.7064T)(c_{\text{Mg}} - c_{\text{Y}})] \quad (13)$$

$$G^{S,\text{ex}} = c_{\text{Gd}} c_{\text{Mg}} [(-33346.6 + 19.3451T) + 13854.0 \times (c_{\text{Gd}} - c_{\text{Mg}})] + c_{\text{Gd}} c_{\text{Y}} (695.1 - 0.3209T) + c_{\text{Mg}} c_{\text{Y}} [(-26612.8 + 13.9461T) + (-2836.2)(c_{\text{Mg}} - c_{\text{Y}})] \quad (14)$$

The thermodynamic model of Mg-Gd-Y ternary alloy was coupled into the phase-field model to reflect the influence of thermodynamics on microstructure.  $f^L$  and  $f^S$  which are significant physical quantity of Eqs.(2)~(5) are written as Eq.(15) and (16) where  $V_m$  is the molar volume of GW103:

$$f^L = (\sum c_{iL} G_i^L + RT \sum c_{iL} \ln c_{iL} + G^{L,\text{ex}}) / V_m \quad (15)$$

$$f^S = (\sum c_{iS} G_i^S + RT \sum c_{iS} \ln c_{iS} + G^{S,\text{ex}}) / V_m \quad (16)$$

### 1.4 Simulation parameters

The microstructure of Mg-Gd-Y system, especially GW103 alloy (Mg-9.27wt%Gd-4.27wt%Y) was simulated and investigated in this work. The initial simulation temperature was 867 K, with the initial undercooling of  $\Delta T = 29$  K. Table 1 gives the simulation parameters of GW103 alloy, where 1 and 2 represent the solute Gd and Y, respectively. Equilibrium solute concentration important to the initial conditions of the simulation varies with temperature, the values of which were calculated based on the thermody-

amic model of Mg-Gd-Y system by PANDAT® software. The liquid diffusion coefficient which varies with temperature was calculated by DICTRA® software. The values of equilibrium solute concentration and liquid diffusion coefficient in solidification temperature interval are shown in Fig.1.

### 1.5 Experimental method

To verify the results of simulation, it is necessary to compare the microstructure and concentration distribution of GW103 alloy obtained by experiments and that by simulation. In this work, several GW103 alloys solidified at different cooling rates were prepared by gravity casting method. GW103 alloys were prepared by pure Mg ingot, Mg-25wt%Gd ingot and Mg-25wt%Y ingot. The ingots

**Table 1 Parameters of GW103 alloy used in the simulation**

Parameters	Value	Ref.
Initial composition, $c_1^0$ /mol%	1.69	-
Initial composition, $c_2^0$ /mol%	1.32	-
Grid size, $\Delta x$ /m	$6.0 \times 10^{-7}$	-
Time step, $\Delta t$ /s	$4.32 \times 10^{-5}$	-
Interface width, $2\lambda$	$4\Delta x$	[38]
Anisotropy strength, $\gamma$	0.025	-
Molar volume, $V_m$ / $\text{m}^3 \cdot \text{mol}^{-1}$	$1.36 \times 10^{-5}$	[38]

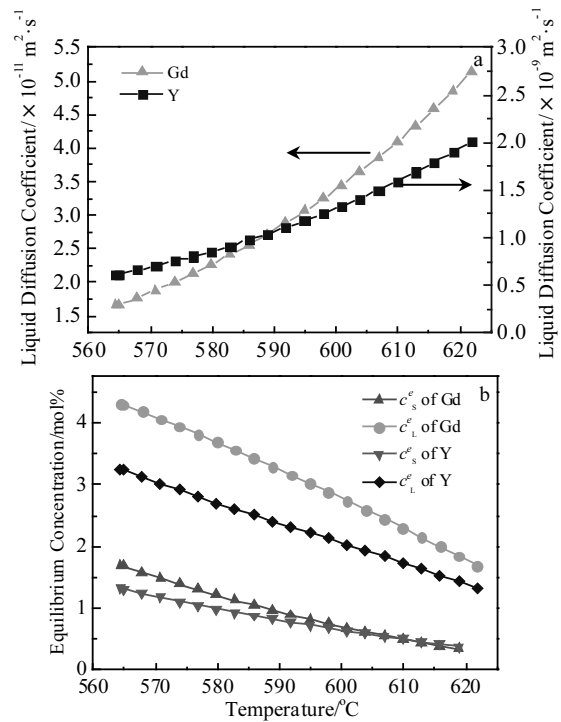


Fig.1 Liquid diffusion coefficient (a) and equilibrium concentration (b) of Gd and Y in solidification temperature interval of GW103

were melted at 750–760 °C with the protection of mixed gas (5% SF<sub>6</sub> and 95% CO<sub>2</sub>). Then the GW103 melt was poured into a permanent mould to produce a step-shaped casting with different wall thickness. With the decrease of the wall thickness, the cooling rate of the GW103 alloy increased. The actual composition of the alloys was Mg-9.27wt%Gd-4.27wt%Y. The detailed preparation method of GW103 can be found in our previous work in Ref.[41].

The microstructure morphology during solidification at different cooling rates was characterized by optical microscope (OM) and a Zeiss Merlin Compact scanning electron microscopy (SEM). The concentration distribution were characterized by an energy dispersive spectrometer (EDS) mounted on the SEM, the principle of which is to use the X-ray photon characteristic energy of different elements for component analysis.

## 2 Results and Discussion

### 2.1 Influence of cooling rate on microstructure and growth kinetics

To investigate the effects of cooling rate on solidification microstructure, one-grain growth and multigrain growth were simulated based on the phase-field model coupled with the thermodynamic model of Mg-Gd-Y alloy and cooling rate. For one-grain simulation case, the grain growth is not influenced by adjacent grains, and dendrite develops freely. Fig.2 shows the dendritic morphology of GW103 alloy in one-grain simulation case at the same time ( $t=10000\Delta t$ ) when dendrites grow at different cooling rates such as 0.0001, 0.0005 and 0.0007 K/ $\Delta t$ . In our previous research, it was found that Mg-Al-Sn alloy exhibited highly developed dendrite arms, clear secondary arms and three-order arms<sup>[32]</sup>. Compared with the dendrite of Mg-Al-Sn alloy we studied previously, the dendrite of GW103 alloy presents sixfold symmetry but does not exhibit fully developed dendritic structure. The dendrite of GW103 alloy exhibits thicker primary dendrite, less secondary arms and even no higher-order arms. The secondary arms of GW103 alloy are not apparent arms, but the small protuberances on the primary dendrite.

Interface energy and liquid diffusion coefficient are sig-

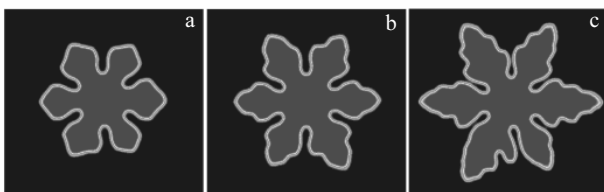


Fig.2 Morphologies of dendrite at 10000 $\Delta t$  under different cooling rates: (a) 0.0001 K/ $\Delta t$ , (b) 0.0005 K/ $\Delta t$ , and (c) 0.0007 K/ $\Delta t$

nificant factors which influence dendrite tip growth kinetics and interface stability, reflecting in the branching ability of primary dendrites. According to the LMK theory in Ref.[42], the radius of the dendrite tip  $\rho$  is proportional to the interface energy. The dendrite tip radius decreases with decreasing the interface energy, which promotes the interface instability and makes for the tendency of side branching. Besides, Ref. [43] proposed an equation to describe the interface stability during casting solidification process:

$$\dot{\epsilon}/\epsilon = -\Gamma\omega^2 - G_T\xi_T + G_L\xi_c \quad (17)$$

Here,  $G_T$  is the conductivity weighted temperature gradient,  $G_L$  is the liquidus temperature gradient, and the quantity  $\xi_c$  is of tiny value which is related to liquid diffusion coefficient of solute. The detailed definitions of quantities in Eq.(17) can be found in Ref.[43].  $\dot{\epsilon}/\epsilon$  is used to evaluate whether the perturbation at interface is stable or not, and the sign of  $\dot{\epsilon}/\epsilon$  determines the interface stability. When  $\dot{\epsilon}/\epsilon < 0$ , it represents that the interface is stable, which is not conducive to dendrite developing. The three terms in the right-hand side of Eq.(17) are determined by interface energy, temperature gradient and solute accumulation ahead of solid/liquid (S/L) interface, respectively. When the interface energy is high, the first term contributes to the tendency of  $\dot{\epsilon}/\epsilon < 0$ . When the liquid solute diffusion coefficient is low, the solute accumulates heavily ahead of S/L interface, and the tiny value of  $G_L\xi_c$  promotes the tendency of  $\dot{\epsilon}/\epsilon < 0$  due to the tiny value of  $\xi_c$ . Therefore, the increasing interface energy and the decreasing liquid solute diffusion coefficient together contribute to interfacial stability, consequently weakening side branching growth. The liquid diffusion coefficient of the main solute in the Mg-Gd-Y and Mg-Al-Sn alloy is on the order of  $10^{-11}$  and  $10^{-9}$ , respectively. The lower liquid diffusion coefficient of solute makes for the tendency of  $\dot{\epsilon}/\epsilon < 0$  and interface stability; therefore, the dendritic morphology of Mg-Gd-Y alloy is less developed than that of Mg-Al-Sn alloy. Besides, the solutes of Mg-Gd-Y alloy diffuse slower in the liquid and accumulate ahead of S/L interface, which increases the interface energy. Both of the high interface energy and good interface stability result in that the dendrites of GW103 alloy exhibit not fully developed morphology.

With the increase of cooling rate, the dendrite is relatively more developed, with larger dendrite size, longer primary dendrite and more secondary arms. The variation of the cooling rate affects the driving force ( $\Delta f$ ), a key factor of impacting microstructure evolution in the phase field model. In the one-grain phase field simulation of GW103, the initial temperature is 867 K, and when temperature descends at different rates, the undercooling in the melt increases at different rates. When the cooling rate is 0.0001, 0.0005 and 0.0007 K/ $\Delta t$ , the undercooling at  $t=10000\Delta t$  is 30, 34 and 36 K, respectively. Higher cooling rate results in higher undercooling in the liquid, thus providing more driving force for dendrite

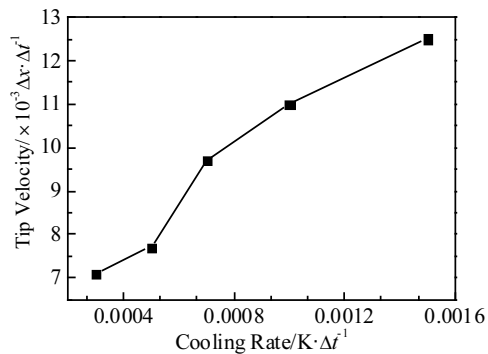


Fig.3 Average tip growth velocity at different cooling rates

growth, which is the reason for ascending tip growth velocity with cooling rate, as illustrated in Fig.3. The ascending tip growth velocity is the reason for larger dendrite size and longer primary dendrite. In addition, the  $S/L$  interface stability decreases as tip growth velocity ascends. For a particular alloy, it was described in the LMK theory that  $v\rho = \text{constant}$  in Ref.[42], and the dendrite tip radius ( $\rho$ ) decreases with the increase of tip growth velocity ( $v$ ). When  $\rho$  decreases to a point where the interface stability could not be kept, the primary dendrite would develop side branching or small protuberances to maintain it<sup>[42]</sup>, as shown in Fig.2c.

For multi-grain simulation case, it is necessary to take nucleation rate into consideration. According to our previous work<sup>[44]</sup>, cooling rate has a great influence on nucleation rate. The increasing cooling rate will increase the undercooling and provide more driving force for nucleation, resulting in more nuclei. When cooling rate is 0.0005  $K/\Delta t$  and 0.0010  $K/\Delta t$ , 9 and 25 grains are set in the simulation domain, respectively. Fig.4 displays the simulated microstructure when solidified at cooling rate of 0.0005  $K/\Delta t$  and 0.0010  $K/\Delta t$ . Fig.5 presents the experimental results of solidification microstructure at the corresponding cooling rate observed by OM and SEM. It can be seen that the microstructure consists of primary  $\alpha$ -Mg dendrite, the dark area in SEM images, and eutectic in bright interdendritic area. The morphology of dendrite at the same cooling rate obtained by simulation agrees with that by experiments, such as the barely developed dendrite, thick primary arms with sixfold symmetry and small protuberance-like secondary arms, which are exhibited clearly in the SEM images.

The variation of cooling rate has a great influence on microstructure of GW103 alloy, such as grain size and dendritic morphology. Through comparing the microstructure at different cooling rates, the grain size at 0.0005  $K/\Delta t$  and 0.0010  $K/\Delta t$  are about 85 and 55  $\mu\text{m}$ , respectively. It illustrates that the increasing cooling rate makes for the microstructure refinement, presenting smaller grain size at higher cooling rate due to insufficient growth space, since the increasing cooling rate leads to higher nucleation undercool-

ing and then more nuclei are formed. Another characteristic of dendrites growing at higher cooling rate is the under-developed dendrites. It exhibits slimmer primary dendrite and less secondary arms as shown in Fig.4b and Fig.5b. The liquid diffusion coefficient of Gd and Y are low, and the solutes accumulate ahead of the  $S/L$  interface, detailed illustration later. It reduces the liquidus temperature gradient  $G_L$  and then contributes to the tendency of  $\dot{\epsilon}/\epsilon < 0$ . As a consequence, the stability of interface is promoted, so the interface tends to remain planar and the protuberance-like secondary arms become less and even disappear.

## 2.2 Influence of cooling rate on concentration distribution

Since cooling rate influences tip growth velocity and nucleation rate, it can be deduced that cooling rate will influence the concentration distribution of GW103 alloy. Fig.6 shows the simulated concentration distribution of solute Gd and Y at different cooling rates. Fig.7 is the concentration distribution of Gd, Y and Mg by EDS. Comparing the concentration distribution at the same cooling rate, it is apparent that Mg mainly distributes in the dendrite and little in interdendritic area; the distribution of solute Gd and Y are inhomogeneous which tend to aggregate in interdendritic

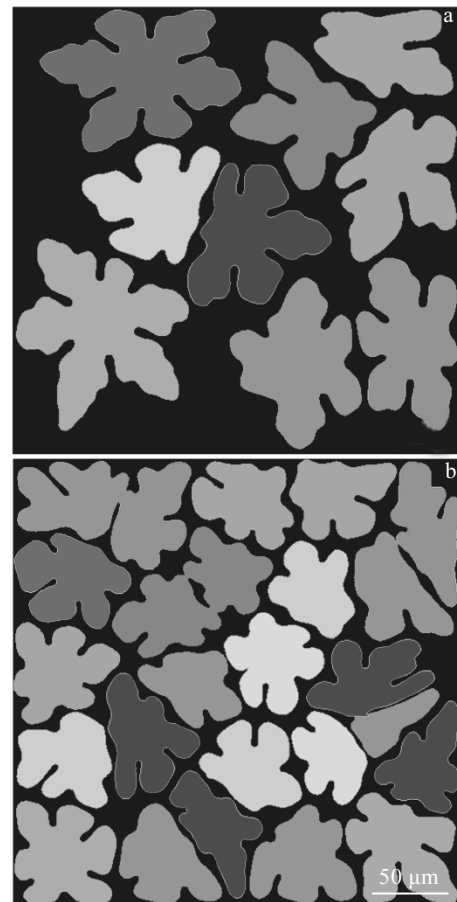


Fig.4 Simulated microstructures at different cooling rates: (a) 0.0005  $K/\Delta t$  and (b) 0.0010  $K/\Delta t$

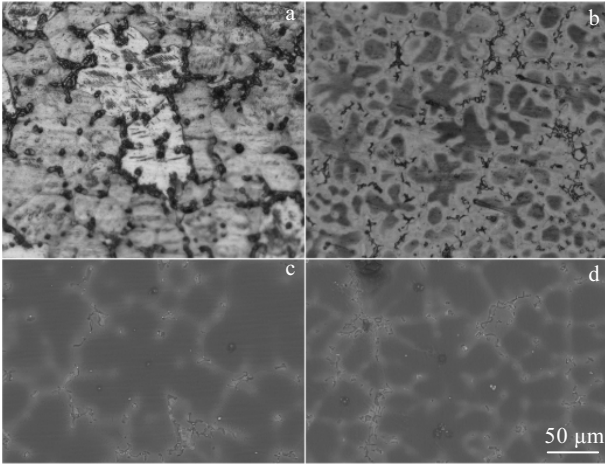


Fig.5 OM (a, b) and SEM (c, d) images of solidification microstructures at different cooling rates: (a, c) 0.0005 K/Δt and (b, d) 0.0010 K/Δt

area. The inhomogeneous distribution of solute Gd and Y can be illustrated more clearly by EDS element line scanning as shown in Fig.8. A linear scanning path from point 'A' to 'E' was generated, which went through two dendritic areas named 'A' and 'E', as well as three interdendritic areas named 'B', 'C' and 'D'. The  $x$ -axis and  $y$ -axis of Fig.8b~8d represent relative position and peak intensity of the corresponding solute, respectively. The peak intensity qualitatively manifests the relative solute content to some degree. As shown in Fig.8c and 8d, it further demonstrates that solute Gd and Y are more likely to accumulate in interdendritic area such as area B, C and D. Moreover, when compared with Y, the peaks of solute Gd are more apparent and the peak width is narrower at B, C and D. It illustrates that the interdendritic solute enrichment of Gd is severer than that of Y. The cooling rate affects the concentration distribution. Solute Gd and Y become more heavily enriched in interdendritic area with the increase of cooling rate.

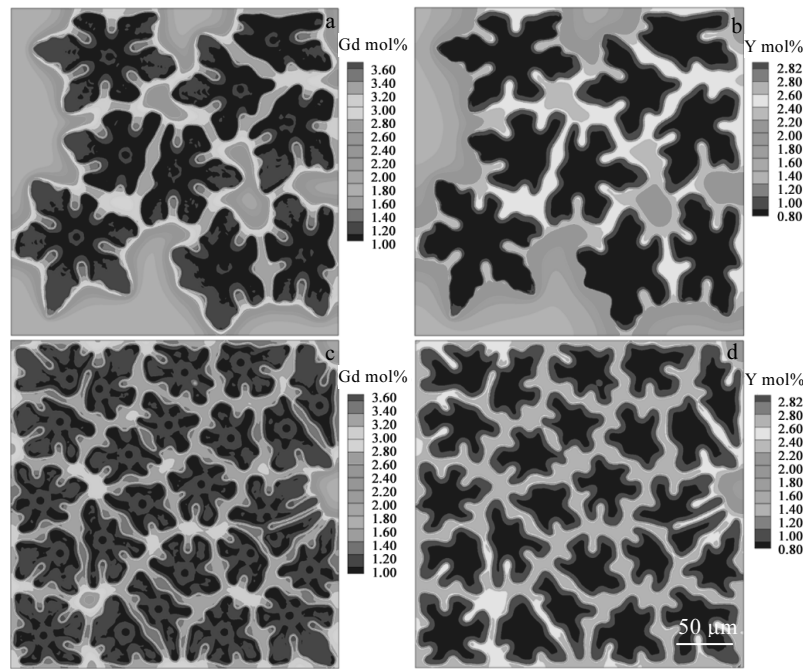


Fig.6 Simulated concentration distribution of solute Gd and Y at different cooling rates: (a, b) 0.0005 K/Δt and (c, d) 0.0010 K/Δt

The solute segregation is significantly influenced by equilibrium partition coefficient  $k$ , an important physical quantity expressed as  $k = c_S^e/c_L^e$ . It reflects the solute redistribution ability at  $S/L$  interface during the solidification process. If the solubility of an element in the solid is lower than that in the liquid, the solutes are rejected to the liquid near the  $S/L$  interface during solidification process, and the solutes accumulate in the later solidified liquid, resulting in solute enrichment in interdendritic areas. Fig.9 displays that

$k_{Gd} < k_Y$  in the solidification temperature interval. It means that the solute Gd more likely remains in liquid and dendritic edge than Y, where consequently Gd accumulates more heavily.  $k_{Gd}$  and  $k_Y$  were calculated based on the  $c_S^e$  and  $c_L^e$  of Gd and Y shown in Fig.1b. In addition to lower equilibrium partition coefficient, as displayed in Fig.1a, the liquid diffusion coefficient of Gd is also much lower (about 2 orders of magnitude) than that of Y, which likewise leads to its severer segregation.

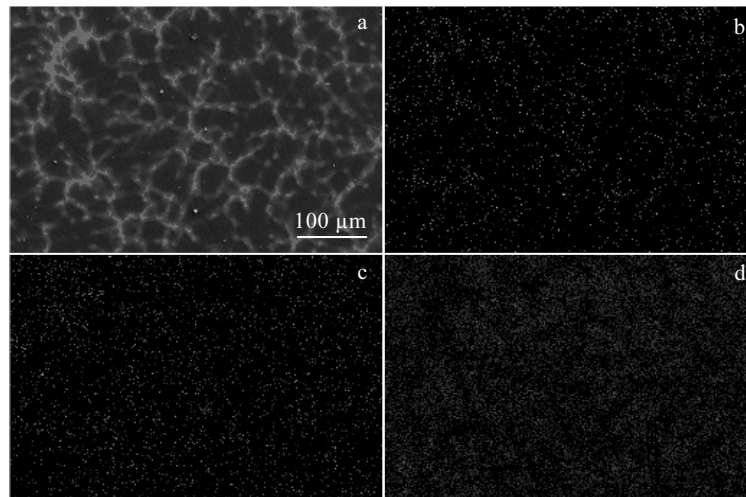


Fig.7 SEM image of characterized region (a) and EDS element distribution (b~d) at high cooling rate: (b) Gd, (c) Y, and (d) Mg

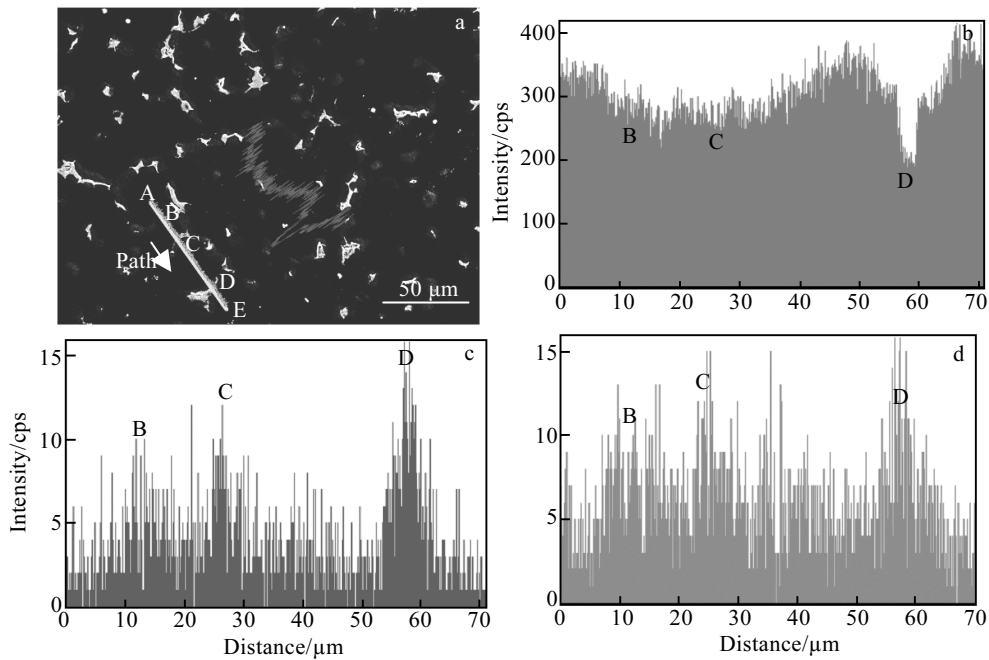


Fig.8 SEM image (a) and EDS element line scanning (b~d): (b) Mg, (c) Gd, and (d) Y

The solidification becomes more deviated from equilibrium with the increase of cooling rate. The concentration characteristics at higher cooling rate can be attributed to two factors, higher tip growth velocity and lower diffusion coefficient. At higher cooling rate (0.0010 K/Δt), more solutes are rejected to the interface of solid and liquid phase due to the increased tip growth velocity. Besides, liquid diffusion coefficients of Gd and Y decrease with the decline of temperature, and they are lower at higher cooling rate. Moreover, there is shorter solidification time under high cooling rate, resulting in less available time for solute diffusion. Therefore, the increasing cooling rate aggravates the solute enrichment and inhomogeneous distribution of solutes.

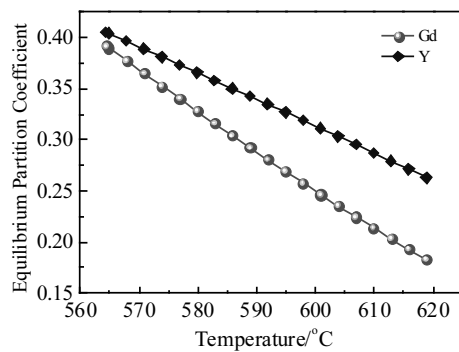


Fig.9 Equilibrium partition coefficient of Gd and Y

### 3 Conclusions

1) GW103 alloy does not exhibit fully developed dendrite. Instead, it exhibits thick sixfold primary dendrite, a few protuberance-like secondary arms and even no higher-order arms, which is distinct from that of Mg-Al-Sn alloy we studied previously.

2) In one-grain simulation case, the dendrite grows freely, and the high cooling rate promotes the growth of dendrite, resulting in increased tip growth velocity and relatively more developed dendrite, exhibiting larger dendrite size, longer primary dendrite and more secondary arms. In multigrain case, cooling rate has a great influence on grain size and dendritic morphology. Higher cooling rate results in smaller grain size, and attributes to more nuclei and insufficient growth space; as well as slimmer primary dendrite and less secondary arms due to solute accumulation ahead of S/L interface. The multigrain simulation results are in good agreement with experiment results.

3) Phase field simulation and experimental characterization results show that solute Gd and Y distribute inhomogeneously. The solutes are more likely to aggregate in interdendritic area where Gd accumulates more heavily than Y, due to  $k_{Gd} < k_Y$  and  $D_{Gd}^L \ll D_Y^L$ . The cooling rate makes a difference to the inhomogeneous distribution of solute Gd and Y. As cooling rate increases, the distribution of Gd and Y becomes more inhomogeneous and the solute enrichment in interdendritic area is much severer, owing to higher tip growth velocity and lower liquid diffusion coefficient of solutes.

### References

- 1 Taub A I, Luo A A. *MRS Bulletin*[J], 2015, 40(12): 1045
- 2 Gao D M, Li Z J, Han Q Y et al. *Materials Science and Engineering A*[J], 2009, 502(1): 2
- 3 Sachdeva D, Tiwari S, Sundarraj S et al. *Metallurgical and Materials Transactions B*[J], 2010, 41(6): 1375
- 4 Luo A A, Fu P H, Peng L M et al. *Metallurgical and Materials Transactions A*[J], 2012, 43(1): 360
- 5 Dahle A K, Lee Y C, Nave M D et al. *Journal of Light Metals*[J], 2001, 1(1): 61
- 6 Han Z Q, Pan H W, Li Y D et al. *Metallurgical and Materials Transaction B*[J], 2015, 46(1): 328
- 7 Zheng F Y, Wu Y J, Peng L M et al. *Journal of Magnesium and Alloys*[J], 2013, 1(2): 122
- 8 Yuan J, Wang Q D, Yin D D et al. *Materials Characterization*[J], 2013, 78: 37
- 9 Zheng K Y, Zeng X Q, Dong J et al. *Materials Science and Engineering A*[J], 2008, 492(1-2): 185
- 10 He S M, Zeng X Q, Peng L M et al. *Journal of Alloys and Compounds*[J], 2007, 427(1-2): 316
- 11 Gao L, Chen R S, Han E H. *Journal of Materials Science*[J], 2009, 44(16): 4443
- 12 Yin D D, Wang Q D, Boehlert C J et al. *Materials Science and Engineering A*[J], 2012, 546: 239
- 13 Zhang P, Ding W J, Lindemann J et al. *Materials Chemistry and Physics*[J], 2009, 118(2-3): 453
- 14 Pang S, Wu G H, Liu W C et al. *Materials Science and Engineering A*[J], 2013, 562: 152
- 15 Zhou J X, Yang Y S, Tong W H et al. *Rare Metal Materials and Engineering*[J], 2010, 39(11): 1899
- 16 Lewis R W, Han Z Q, Gethin D T. *Comptes Rendus Mecanique*[J], 2007, 335(5-6): 287
- 17 Han Z Q, Zhu W, Liu B Q. *Acta Metallurgica Sinica*[J], 2009, 45(3): 356
- 18 Huo L, Han Z Q, Liu B C. *Acta Metallurgica Sinica*[J], 2009, 45(12): 1414
- 19 Su B, Han Z Q, Liu B C. *ISIJ International*[J], 2013, 53(3): 527
- 20 Han G M, Han Z Q, Luo A A et al. *Scripta Materialia*[J], 2013, 68(9): 691
- 21 Han G M, Han Z Q, Luo A A et al. *Metallurgical and Materials Transactions A*[J], 2015, 46(2): 948
- 22 Han Z Q, Han G M, Luo A A et al. *Computational Materials Science*[J], 2015, 101: 248
- 23 Provatas N, Elder K. *Phase-Field Methods in Materials Science and Engineering*[M]. Weinheim: John Wiley & Sons, 2011
- 24 Kim S G. *Acta Materialia*[J], 2007, 55(13): 4391
- 25 Karma A. *Physical Review Letters*[J], 2001, 87(11): 115 701
- 26 Zhu J Z, Liu Z K, Vaithyanathan V et al. *Scripta Materialia*[J], 2002, 46(5): 401
- 27 Liu H, Gao Y, Zhu Y M et al. *Acta Materialia*[J], 2014, 77: 133
- 28 Xing H, Ankit K, Dong X L et al. *International Journal of Heat and Mass Transfer*[J], 2018, 117: 1107
- 29 Xing H, Zhang L M, Song K K et al. *International Journal of Heat and Mass Transfer*[J], 2017, 104: 607
- 30 Yang C, Xu Q Y, Liu B C. *Journal of Materials Science*[J], 2018, 53(13): 9755
- 31 Shang S, Han Z Q. *Journal of Materials Science*[J], 2019, 54(4): 3111
- 32 Shang S, Han Z Q, Luo A A. *Materials Science and Technology*[J], 2018, 34(11): 1362
- 33 Kim S G, Kim W T, Suzuki T. *Physical Review E*[J], 1999,

- 60(6): 7186
- 34 Kim S G, Kim W T, Suzuki T et al. *Journal of Crystal Growth*[J], 2004, 261(1): 135
- 35 Eiken J, Böttger B, Steinbach I. *Physical Review E*[J], 2006, 73(6): 066 122
- 36 Echebarria B, Folch R, Karma A et al. *Physical Review E*[J], 2004, 70(6): 061 604
- 37 Ode M, Lee J S, Kim S G et al. *ISIJ International*[J], 2000, 40(9): 870
- 38 Pan H W, Han Z Q, Liu B C. *Journal of Materials Science and Technology*[J], 2016, 32(1): 68
- 39 Saunders N. *Calphad*[J], 1990, 14(1): 61
- 40 Guo C P, Du Z M, Li C R. *Calphad*[J], 2007, 31(1): 75
- 41 Wu K Y, Wang X Y, Xiao L et al. *Advanced Engineering Materials*[J], 2018, 20(3):1 700 717
- 42 Langer J S, Müller-Krumbhaar H. *Acta Metallurgica*[J], 1978, 26(11):1681
- 43 Stefanescu D M. *Science and Engineering of Casting Solidification Third Edition*[M]. Switzerland: Springer International Publishing, 2015:152
- 44 Wang X Y, Wang F F, Wu K Y et al. *Rare Metals*[J], 2019(6): 1

## 冷却速率对 Mg-Gd-Y 三元镁合金凝固组织影响的相场模拟

赵雪婷<sup>1,2</sup>, 尚 闪<sup>1,2</sup>, 张天向<sup>1,2,3</sup>, 张瑞杰<sup>3</sup>, 王先飞<sup>4</sup>, 李中权<sup>4</sup>, 韩志强<sup>1,2</sup>

(1. 清华大学 材料学院, 北京 100084)

(2. 清华大学 先进成形制造教育部重点实验室, 北京 100084)

(3. 北京科技大学 钢铁共性技术协同创新中心, 北京 100083)

(4. 上海航天精密机械研究所, 上海 201600)

**摘要:** 结合 Mg-Gd-Y 体系热、动力学模型, 首次考虑冷却速率, 建立了 Mg-Gd-Y 三元镁合金的相场模型。应用该模型模拟了 GW103 (Mg-1.69%Gd-1.32%Y, 摩尔分数) 合金在不同冷却速率下的凝固组织微观形貌和成分分布。采用重力铸造法制备 GW103 合金并对其进行试验表征以验证相场模型。结果表明, GW103 合金呈不发达枝晶形貌且一次枝晶臂具六次对称性, 二次枝晶臂呈突起状且无更高次枝晶臂。在多晶粒相场模拟中, 随着冷却速率的增加, GW103 微观组织细化, 晶粒尺寸减小、一次枝晶臂变细、二次枝晶臂数目减少。较高的冷却速率加剧了 Gd 和 Y 在枝晶间的溶质富集现象, 令成分分布更不均匀。

**关键词:** 相场; 模拟; 镁; 微观结构; 冷却速率

作者简介: 赵雪婷, 女, 1995 年生, 硕士生, 清华大学材料学院, 北京 100084, 电话: 010-62794482, E-mail: zhaoxt17@tsinghua.org.cn